IET Electric Power Applications

Research Article

IET Journals
The Institution of Engineering and Technology

Interturn short-circuit fault diagnosis in PMSM with partitioned stator windings

ISSN 1751-8660
Received on 3rd February 2020
Revised 9th July 2020
Accepted on 5th August 2020
doi: 10.1049/iet-epa.2020.0080
www.ietdl.org

Manuel Armando Mazzoletti[1] ✉, *Guillermo R. Bossio*[2], *Cristian Hernan De Angelo*[2]

[1]*Research and Development Laboratory on Electrical Energy, National University of Misiones, Ruta Nac. #12, km 7.5, Misiones, Argentina*
[2]*IITEMA-CONICET, GEA-UNRC, Ruta Nac. #36, km 601, Río Cuarto, Córdoba, Argentina*
✉ *E-mail: armando.mazzoletti@gmail.com*

Abstract: A new signal-based strategy for stator winding interturn short-circuit fault detection and isolation in permanent magnet synchronous machines (PMSM) is proposed. The strategy is based on an analysis of the midpoint voltage of the phase windings. A PMSM model with partitioned stator windings including an interturn short-circuit fault is presented. Unlike the motor current signature analysis methods, the midpoint voltage measurement allows detecting an incipient stator fault even under external disturbances without false alarms. For PMSM generators used in variable-speed wind turbines, the random changes of wind produce fluctuations in the rotor speed. In this situation, conventional fault detection methods used for the steady-state condition may produce errors in the fault diagnosis. However, the proposed strategy is capable of rejecting the effects of the non-stationary speed conditions by resampling the voltage signals at fixed increments of the rotor angular position. Several experimental results in time and frequency-domain are presented for different speed conditions using a PMSM with modified stator winding.

1 Introduction

Permanent magnet synchronous machines (PMSMs) are used in several applications that require a precise torque control under different operating conditions [1]. In PMSMs, the magnetic flux induced on the stator windings is generated by the permanent magnets, thus avoiding the brushes and rotor windings commonly used in conventional synchronous motors. Unlike the ferrite or AlNiCo magnets, both surface-mounted and interior permanent magnet rotors are formed by rare-earth magnets such as SmCo and NdFeB significantly improve the magnetic flux density and consequently, the efficiency and power density also increase [2].

Wind energy conversion systems (WECSs) use different configurations of the power electronic systems to control the connection of the PMSM generator to the grid [3, 4]. According to the wind turbine shaft connection to the PMSM, WECS can be classified as indirect-drive or direct-drive. The direct-drive WECS allows the PMSM to be coupled directly to the variable-speed wind turbine, thus the system reliability is increased due to mechanical gearboxes are eliminated. Generally, WECSs are installed outside urban centres or in difficult access areas, e.g. offshore wind turbines. Owing to this, the repair of defective components becomes a difficult operation with high-maintenance costs. In these situations, condition monitoring systems (CMSs) are useful in recognising and indicating anomalies in WECSs behaviour [5].

Insulation of the stator windings is the major source of failure in electrical machines [6]. The progressive degradation of the insulation may cause damage between the turns producing a rapid overheat into the stator winding [7]. As a result, a large current flows through the short-circuited turns that impairs the magnetic coercivity and produce partial demagnetisation of the permanent magnets due to located magnetic flux [8]. Furthermore, if the temperature of the magnet exceeds the threshold of the Curie temperature, its magnetisation is reduced to zero [9]. Therefore, CMS is able to detect interturn short-circuit faults that are essential to avoid catastrophic failures such as phase to phase or phase to ground faults.

Most of the machine faults (e.g. stator, rotor, and bearing faults) affect or modify current or voltage waveforms. Thus, signal-based fault diagnosis strategies that use the measurement of electrical signals are suitable for CMS of electric machines. Among them, motor current/voltage signature analysis (MCSA/MVSA) techniques are based on the monitoring of the stator current or voltage spectra for faults detection [10, 11]. However, different faults may produce similar effects in the spectrum of the electrical signals [12]. Even more, other perturbations such as rotor speed fluctuations or converter faults can also introduce variation in the current signatures, making difficult the identification of incipient faults. Hence, fault isolation involves a thorough analysis of the measured signals to obtain a correct diagnosis [13].

Several signal-based fault-detection techniques were proposed for the monitoring of specific harmonic components into the current and voltage signals measurement [14–18]. A comprehensive analysis of the effects of interturn faults with different winding configurations is performed in [19]. According to [15, 19], the third and ninth harmonic component of the stator current, likewise, the first, fifth, and seventh harmonic component of the zero-sequence voltage component (ZSVC) can be monitored to recognise such faults. For implementing the ZSVC-based methods, the neutral point connection of the windings and an external balanced resistor network are required. This external resistor network is used to reject electronic inverter effects. To avoid the false diagnosis due to the unbalance of the resistance network, a tolerance range for the resistances is defined.

The interturn short-circuit fault in a PMSM generator is analysed in [20]. In this case, the interturn short-circuit fault produces an unbalanced back electromotive force (EMF) on the phase windings. This condition is exacerbated further for high shaft speed and the increased fault severity. Since such strategies are proposed for steady-state operation, variable speed wind turbine operation can produce false alarms. Non-stationary state operation has been considered in several fault detection techniques. The harmonic components in the stator currents spectra and ZSVC are monitored based on several filtering order tracking (OT) algorithms such as wavelet transform [21, 22], Wigner Ville analysis [23], and the Vold–Kalman filter [24], among others. Most of these methods are based on selective filters to isolate the specific frequency component associated with the fault.

On the other hand, different PMSM faults such as the partial demagnetisation or breakage of the magnet cause distortion in the waveform of the back EMF. Additionally, other problems such as rotor speed fluctuations, motor asymmetries, unbalanced voltages or load imbalance, can also produce the same components in the EMF or phase currents, thus making the diagnosis more difficult.

Therefore, to make a correct fault diagnosis in PMSM, Da *et al.* [25] proposed a method based on search coils wound around armature teeth to detect faults through direct flux measurement. Zeng *et al.* [26] proposed a method based on a similar approach to improve the sensitivity for detecting interturn short-circuit faults at an early stage. Regardless of any of them, the search coils around each tooth require the modification of the windings. Furthermore, the methods based on search coils also require a complex data acquisition system for practical implementation. In this sense, signal processing increases with the number of armature teeth. Although this technique is invasive, it is suitable in applications where the fault condition of the PMSM could lead to very high repair or replacement costs such as in the case of the WECS, aerospace, and automotive industry, among other critical applications.

In this paper, a new signal-based strategy for interturn short-circuit fault diagnosis in PMSM with partitioned stator windings is proposed. Since that several perturbations can produce variations in the phase voltage such as the faults on the generator-side converter, effects of the variable wind turbine speed, among others, fault detection is performed by a residual voltage (RV) obtained from the difference between midpoint voltages measured on the semi-windings of each stator phase. To decouple the effects of the variable wind turbine speed, the voltage signals are resampled at fixed increments of the rotor shaft position.

Therefore, the following features can be highlighted in this work:

(i) a new PMSM dynamic model with partitioned stator windings including an interturn short-circuit fault in any phase-windings;
(ii) unlike other strategies that analyse the stator fault on the complete phase windings based on MCSA/MVSA, an interturn short circuit fault can be detected and isolated by condition monitoring of only one RV of the three-phase stator windings, even for power supply unbalanced voltages or asymmetric loads;
(iii) the decoupling of the effects of the variable wind turbine speed is realised by the resampling of stator voltage at fixed increments of the rotor shaft position;
(iv) the angular speed is estimated by using the measured stator voltages, avoiding the use of an external position or speed sensor.

Experimental results in time-domain and frequency-domain under different stator fault severity and non-stationary operation conditions using a PMSM with modified winding are presented. The three-phase PMSM prototype allows access to the midpoints of the phase windings and also to intermediate taps connections for short-circuiting of turns.

2 PMSM models with partitioned windings including an interturn short-circuit fault

An electrical scheme of the PMSM with partitioned stator windings including an interturn short-circuit fault in the *a*-phase winding is shown in Fig. 1. It can be assumed that the *a*-phase winding is formed by two circuits connected in series (two semi-windings). Ideally, the semi-windings are formed by the resistor of value $r_s/2$ and the magnetising inductance of $N_s/2$ turns. Thus, the voltage, v_{as}, on the phase stator-windings can be obtained by adding the voltage: $v_{a1} + v_{a2}$; where the subscript 1 indicates the voltage measured from the neutral point of the winding, '*n*', to the midpoint of the phase winding, '*o*' (semi-winding 1), and the subscript 2 is the voltage measured from the midpoint of phase windings to the end of a phase winding, *'a'* (semi-winding 2). Such semi-windings differ from one another since that one of them is affected by an interturn short-circuit fault.

Additionally, the contact resistance between the shorted turns is represented by the fault resistance, r_f. The fault severity is denoted by μ, which is the ratio between the number of shorted turns and the number of turns of the faulty semi-windings. Hence, for a healthy PMSM, $\mu = 0$, otherwise, for a semi-winding completely shorted, $\mu = 1$. In this situation, the semi-winding with damaged turns (faulty semi-winding 2) can be modelled by the resistor $\mu r_s/2$

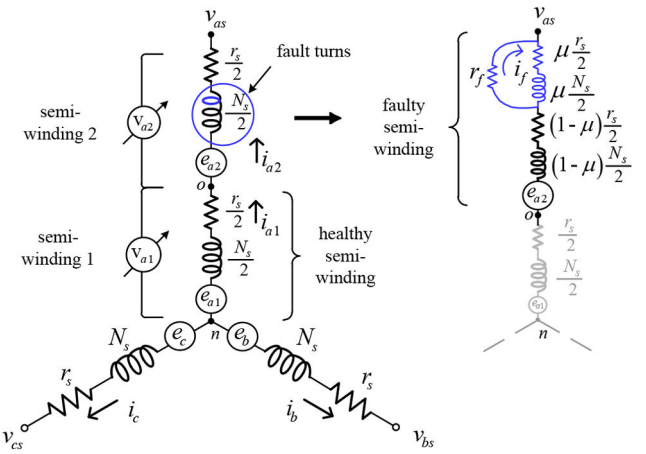

Fig. 1 *Scheme of the partitioned stator winding of a PMSM with an interturn short-circuit in the a-phase winding*

and the inductance with $\mu N_s/2$ turns. According to the fault severity, the magnitudes of the resistor and magnetising inductance are reduced to $(1-\mu)$. Meanwhile, the fault resistor reduction increases the severity since a greater current i_f is circulating into damaged turns. The model of the semi-windings without damaged turns is not modified. Based on these assumptions, the extended PMSM model with stator fault is developed.

2.1 Stator fault in a-phase winding

The PMSM dynamic model with partitioned stator windings that allows us to include the effects of the interturn short-circuit fault in any phase windings is derived similar to [27]. The PMSM dynamic model including an interturn short-circuit fault in the *a*-phase winding is given by

$$\boldsymbol{v}_{\mathrm{f},abc} = \boldsymbol{R}_{\mathrm{f}a}\boldsymbol{i}_{\mathrm{f},abc} + p\boldsymbol{L}_{\mathrm{f}a}\boldsymbol{i}_{\mathrm{f},abc} + \boldsymbol{e}_{\mathrm{pm},\mathrm{f}a}, \tag{1}$$

where $\boldsymbol{v}_{\mathrm{f},abc} = [v_{a1}\ v_{a2}\ v_{b1}\ v_{b2}\ v_{c1}\ v_{c2}\ 0]^{\mathrm{T}}$ is the voltage vector, $\boldsymbol{i}_{\mathrm{f},abc} = [i_{a1}\ i_{a2}\ i_{b1}\ i_{b2}\ i_{c1}\ i_{c2}\ i_{\mathrm{f}}]^{\mathrm{T}}$ is the current vector, $\boldsymbol{e}_{\mathrm{pm},\mathrm{f}a} = [e_{a1}\ e_{a2}\ e_{b1}\ e_{b2}\ e_{c1}\ e_{c2}\ e_{\mathrm{f}}]^{\mathrm{T}}$ is the induced back-EMF vector and $p = d/dt$.

The flux linkage, $\boldsymbol{\Psi}_{\mathrm{pm},\mathrm{f}a}$, may be expressed as follows:

$$\boldsymbol{\Psi}_{\mathrm{pm},\mathrm{f}a} = \frac{1}{2}\psi_{\mathrm{pm}}\begin{bmatrix}\sin\theta_{\mathrm{r}}\\ \sin\theta_{\mathrm{r}}\\ \sin(\theta_{\mathrm{r}}-2\pi/3)\\ \sin(\theta_{\mathrm{r}}-2\pi/3)\\ \sin(\theta_{r}+2\pi/3)\\ \sin(\theta_{\mathrm{r}}+2\pi/3)\\ -\mu\sin\theta_{\mathrm{r}}\end{bmatrix}, \tag{2}$$

where ψ_{pm} and θ_{r} are the amplitude of the permanent magnet flux and the instantaneous rotor position, respectively.

Deriving (2), the induced back-EMFs are calculated as follows:

$$\boldsymbol{e}_{\mathrm{pm},\mathrm{f}a} = \frac{1}{2}\psi_{\mathrm{pm}}\omega_{\mathrm{r}}\begin{bmatrix}\cos\theta_{\mathrm{r}}\\ \cos\theta_{\mathrm{r}}\\ \cos(\theta_{\mathrm{r}}-2\pi/3)\\ \cos(\theta_{\mathrm{r}}-2\pi/3)\\ \cos(\theta_{r}+2\pi/3)\\ \cos(\theta_{\mathrm{r}}+2\pi/3)\\ \mu\cos\theta_{\mathrm{r}}\end{bmatrix}, \tag{3}$$

where the first and second rows of (3) indicate the induced back-EMF for a-phase semi-winding defined by $e_{a1} = e_{a2} = 1/2\psi_{pm}\omega_r \cos\theta_r$ (see both semi-windings in Fig. 1).

The stator inductances matrix, $\boldsymbol{L}_{fa}$, and resistances matrix, $\boldsymbol{R}_{fa}$, which include the modified parameters due to the interturn short-circuit fault within semi-windings of the a-phase are defined in (4) and (5), respectively (see (4)) , where $L_s = L_{ls} + L_M$; the winding coupling factors are $a = -(\sqrt{3}/4) - (\pi/3)$ and $b = (\sqrt{3}/4) - (\pi/6)$

$$\boldsymbol{R}_{f_a} = \frac{1}{2}\begin{bmatrix} r_s & 0 & 0 & 0 & 0 & 0 & 0 \\ 0 & r_s & 0 & 0 & 0 & 0 & -\mu r_s \\ 0 & 0 & r_s & 0 & 0 & 0 & 0 \\ 0 & 0 & 0 & r_s & 0 & 0 & 0 \\ 0 & 0 & 0 & 0 & r_s & 0 & 0 \\ 0 & 0 & 0 & 0 & 0 & r_s & 0 \\ 0 & -\mu r_s & 0 & 0 & 0 & 0 & \mu r_s + 2r_f \end{bmatrix}. \tag{5}$$

The self and mutual inductances of PMSM are calculated as indicated in Corollary 1.

Corollary 1: The inductances of PMSM dynamic model may be calculated as [28]

$$L_{xy} = \mu_0 rl \int_0^{2\pi} \frac{w_x(\phi_m) w_y(\phi_m)}{g(\phi_m)} \mathrm{d}\phi_m, \tag{6}$$

where the winding functions, w_x and w_y, are continuous functions of the position, which can be position relative to the stator, ϕ_m, for stator winding. g is the air gap function, r is the radio, l is the axial length of the machine, and μ_0 is the permeability of free space.

More details about the self- and mutual-inductances and the winding coupling factors, 'a' and 'b', see the Appendix.

Note that the phase voltage for any stator winding is defined by $v_x = v_{x1} + v_{x2}$. For the case, $\mu = 0$, adding the voltages on the right of (1) correspond to the healthy PMSM [28]. On the other hand, for $\mu \neq 0$, adding voltages, $v_a = v_{a1} + v_{a2}$, define the faulty PMSM dynamic model for a-phase winding, similar to [27]. However, the difference between the measured voltage results as

$$v_{RVa} = v_{a1} - v_{a2}, \tag{7}$$

where v_{RVa}, is the RV of the phase a.

Therefore, knowing that $i_x = i_{x1} = i_{x2}$ for any stator phase winding, (7) may be expressed as

$$\begin{aligned} v_{RVa} = {} & \frac{r_s}{2} i_a + \frac{L_s}{2} p i_a + (a+b)\frac{L_M}{2} p i_b + (b+a)\frac{L_M}{2} p i_c + e_{a1} \\ & - \frac{r_s}{2} i_a - \frac{L_s}{2} p i_a - (b+a)\frac{L_M}{2} p i_b - (a+b)\frac{L_M}{2} p i_c - e_{a2} \\ & + \mu\left(\frac{r_s}{2} i_f + \frac{L_s}{2} p i_f\right). \end{aligned} \tag{8}$$

From (8) it can be seen that the voltages drop due to stator resistance, r_s, leakage and magnetising inductance, L_{ls}, L_M, are equals in both semi-winding voltages.

Finally, (8) may now be expressed as

$$v_{RVa} = \mu\left(\frac{r_s}{2} + \frac{L_s}{2} p\right) i_f. \tag{9}$$

This highlighted feature implies that the RV is proportional to the fault severity, μ, and the fault current, i_f. In other words, the RV is independent of the phase currents, allowing isolating the external effects of unbalanced voltages or imbalanced loads.

The RV for b-phase winding is obtained by the difference between the third and fourth rows of the faulty PMSM dynamic model in (1)

$$\begin{aligned} v_{RVb} = {} & \frac{r_s}{2} i_b + (a+b)\frac{L_M}{2} p i_a + \frac{L_s}{2} p i_b + (b+a)\frac{L_M}{2} p i_c \\ & + \frac{1}{2}\mu 2 a L_M p i_f + e_{b1} - \frac{r_s}{2} i_b - (b+a)\frac{L_M}{2} p i_a - \frac{L_s}{2} p i_b \\ & - (a+b)\frac{L_M}{2} p i_c - e_{b2} - \frac{1}{2}\mu 2 b L_M p i_f, \end{aligned} \tag{10}$$

where the back-EMF for b-phase winding is defined by $e_{b1} = e_{b2} = 1/2\psi_{pm}\omega_r \cos(\theta_r - 2\pi/3)$ [see in (3)].

Finally, by eliminating all equal terms, the RV can be written as follows:

$$\begin{aligned} v_{RVb} &= \frac{1}{2}\mu 2 (a-b) L_M p i_f \\ &= \mu\left(-\frac{\sqrt{3}}{2} - \frac{\pi}{6}\right) L_M p i_f. \end{aligned} \tag{11}$$

Similar, the RV for c-phase winding obtained through the difference between the fifth and sixth rows of (1) can be written as

$$\begin{aligned} v_{RVc} &= \frac{1}{2}\mu 2 (b-a) L_M p i_f \\ &= \mu\left(\frac{\sqrt{3}}{2} + \frac{\pi}{6}\right) L_M p i_f. \end{aligned} \tag{12}$$

Note that an interturn fault on the a-phase winding produces three RVs, even when the b- and c-phase windings are healthy. This additional RVs on the healthy windings are due to linked magnetic fluxes generated by the fault current circulating in faulty turns. The RV obtained from (9), (11), and (12) are similar to the voltage signals obtained by Hang *et al.* [16] from the mathematical ZSVC-based model. Therefore, if the high-order harmonic components are neglected, from (9) the fault current for the steady-state can be expressed as follows:

$$\tilde{I}_f = \frac{\tilde{V}_{RVa}}{\mu((r_s/2) + j\omega_e(L_s/2))}, \tag{13}$$

where

$$\begin{cases} \left|\tilde{I}_f\right| = \dfrac{\left|\tilde{V}_{RVa}\right|}{\mu\left|((r_s/2) + j\omega_e(L_s/2))\right|} \\ \theta_{I_f} = \theta_{RVa} - \varphi_a \\ \varphi_a = \mathrm{atan2}(\omega_e L_s, r_s) \end{cases}$$

$$\boldsymbol{L}_{f_a} = \frac{1}{2}\begin{bmatrix} L_s & 0 & aL_M & bL_M & bL_M & aL_M & 0 \\ 0 & L_s & bL_M & aL_M & aL_M & bL_M & -\mu L_s \\ aL_M & bL_M & L_s & 0 & bL_M & aL_M & \mu 2 a L_M \\ bL_M & aL_M & 0 & L_s & aL_M & bL_M & \mu 2 b L_M \\ bL_M & aL_M & aL_M & bL_M & L_s & 0 & \mu 2 b L_M \\ aL_M & bL_M & bL_M & aL_M & 0 & L_s & \mu 2 a L_M \\ 0 & -\mu L_s & \mu 2 a L_M & \mu 2 b L_M & \mu 2 b L_M & \mu 2 a L_M & \mu L_{ls} + \mu^2 L_M \end{bmatrix}, \tag{4}$$

where $\tilde{I}$ and $\tilde{V}$ are the fundamental components of the current and voltage, respectively. ω_e is the synchronous angular speed.

It can be seen that the initial phase angle of the fault current, θ_{I_f}, is approximately equal to that of the phase angle of θ_{RVa} for $\mu \neq 0$.

On the other hand, (11) can be expressed by

$$\tilde{V}_{RVb} = \mu\left(-\frac{\sqrt{3}}{2} - \frac{\pi}{6}\right)j\omega_e L_M \tilde{I}_f, \tag{14}$$

where

$$\begin{cases} \left|\tilde{V}_{RVb}\right| = \left|\mu\left(-\frac{\sqrt{3}}{2} - \frac{\pi}{6}\right)\omega_e L_M\right|\left|\tilde{I}_f\right| \\ \theta_{RVb} = \theta_{I_f} + \varphi_b, \text{ with } \varphi_b = \pi/2 \end{cases}$$

and (12) is given by

$$\tilde{V}_{RVc} = \mu\left(\frac{\sqrt{3}}{2} + \frac{\pi}{6}\right)j\omega_e L_M \tilde{I}_f, \tag{15}$$

where

$$\begin{cases} \left|\tilde{V}_{RVc}\right| = \left|\mu\left(\frac{\sqrt{3}}{2} + \frac{\pi}{6}\right)\omega_e L_M\right|\left|\tilde{I}_f\right| \\ \theta_{RVc} = \theta_{I_f} + \varphi_c, \text{ with } \varphi_c = \pi/2 \end{cases}$$

It can be seen that the phase angles θ_{RVb} and θ_{RVc} are approximately equal to that of the phase angle of θ_{I_f} that hold the phase angle information of *a*-phase faulty winding. In other words, once the interturn fault is triggered, all RVs holds the information about the faulty winding. This characteristic allows us to detect and locate an incipient stator fault from any RV, even if the midpoint of the faulty winding is not available.

2.2 Stator fault in b- and c-phase winding

PMSM dynamic models that allow us to include an interturn short-circuit fault in the other phases are developed, similar to the previous section. Therefore, in the present section, only the stator resistances matrix, $\boldsymbol{R}_{fb}$ and $\boldsymbol{R}_{fc}$, the stator inductances matrix, $\boldsymbol{L}_{fb}$ and $\boldsymbol{L}_{fc}$, also the flux linkage of the *b*- and *c*-phase, respectively, are exposed. Note that the terms corresponding to the fault changes according to the faulty phase. Therefore, the PMSM models for each faulty phase is obtained by replacing in (1) the corresponding matrices

$$\boldsymbol{R}_{f_b} = \frac{1}{2}\begin{bmatrix} r_s & 0 & 0 & 0 & 0 & 0 & 0 \\ 0 & r_s & 0 & 0 & 0 & 0 & 0 \\ 0 & 0 & r_s & 0 & 0 & 0 & 0 \\ 0 & 0 & 0 & r_s & 0 & 0 & -\mu r_s \\ 0 & 0 & 0 & 0 & r_s & 0 & 0 \\ 0 & 0 & 0 & 0 & 0 & r_s & 0 \\ 0 & 0 & 0 & -\mu r_s & 0 & 0 & \mu r_s + 2r_f \end{bmatrix}. \tag{16}$$

$$\boldsymbol{R}_{f_c} = \frac{1}{2}\begin{bmatrix} r_s & 0 & 0 & 0 & 0 & 0 & 0 \\ 0 & r_s & 0 & 0 & 0 & 0 & 0 \\ 0 & 0 & r_s & 0 & 0 & 0 & 0 \\ 0 & 0 & 0 & r_s & 0 & 0 & 0 \\ 0 & 0 & 0 & 0 & r_s & 0 & 0 \\ 0 & 0 & 0 & 0 & 0 & r_s & -\mu r_s \\ 0 & 0 & 0 & 0 & 0 & -\mu r_s & \mu r_s + 2r_f \end{bmatrix}. \tag{17}$$

$$\boldsymbol{L}_{f_b} = \frac{1}{2}$$

$$\begin{bmatrix} L_s & 0 & aL_M & bL_M & bL_M & aL_M & \mu 2aL_M \\ 0 & L_s & bL_M & aL_M & aL_M & bL_M & \mu 2bL_M \\ aL_M & bL_M & L_s & 0 & bL_M & aL_M & 0 \\ bL_M & aL_M & 0 & L_s & aL_M & bL_M & -\mu L_s \\ bL_M & aL_M & aL_M & bL_M & L_s & 0 & \mu 2bL_M \\ aL_M & bL_M & bL_M & aL_M & 0 & L_s & \mu 2aL_M \\ \mu 2aL_M & \mu 2bL_M & 0 & -\mu L_s & \mu 2bL_M & \mu 2aL_M & \mu L_{ls} + \mu^2 L_M \end{bmatrix}, \tag{18}$$

$$\boldsymbol{L}_{f_c} = \frac{1}{2}$$

$$\begin{bmatrix} L_s & 0 & aL_M & bL_M & bL_M & aL_M & \mu 2aL_M \\ 0 & L_s & bL_M & aL_M & aL_M & bL_M & \mu 2bL_M \\ aL_M & bL_M & L_s & 0 & bL_M & aL_M & \mu 2bL_M \\ bL_M & aL_M & 0 & L_s & aL_M & bL_M & \mu 2aL_M \\ bL_M & aL_M & aL_M & bL_M & L_s & 0 & 0 \\ aL_M & bL_M & bL_M & aL_M & 0 & L_s & -\mu L_s \\ \mu 2aL_M & \mu 2bL_M & \mu 2bL_M & \mu 2aL_M & 0 & -\mu L_s & \mu L_{ls} + \mu^2 L_M \end{bmatrix}. \tag{19}$$

The flux linkage, $\boldsymbol{\Psi}_{pm,fb}$, may be expressed as

$$\boldsymbol{\Psi}_{pm,fb} = \frac{1}{2}\psi_{pm}\begin{bmatrix} \sin\theta_r \\ \sin\theta_r \\ \sin(\theta_r - 2\pi/3) \\ \sin(\theta_r - 2\pi/3) \\ \sin(\theta_r + 2\pi/3) \\ \sin(\theta_r + 2\pi/3) \\ -\mu\sin(\theta_r - 2\pi/3) \end{bmatrix}, \tag{20}$$

and, flux linkage, $\boldsymbol{\Psi}_{pm,fc}$, may be expressed as

$$\boldsymbol{\Psi}_{pm,fc} = \frac{1}{2}\psi_{pm}\begin{bmatrix} \sin\theta_r \\ \sin\theta_r \\ \sin(\theta_r - 2\pi/3) \\ \sin(\theta_r - 2\pi/3) \\ \sin(\theta_r + 2\pi/3) \\ \sin(\theta_r + 2\pi/3) \\ -\mu\sin(\theta_r + 2\pi/3) \end{bmatrix}, \tag{21}$$

The induced back-EMF is calculated by deriving (20) and (21), similar to (3). Therefore, the PMSM dynamic models with stator fault in the *b*- and *c* phase are expressed by replacing in (1) the matrices exposed.

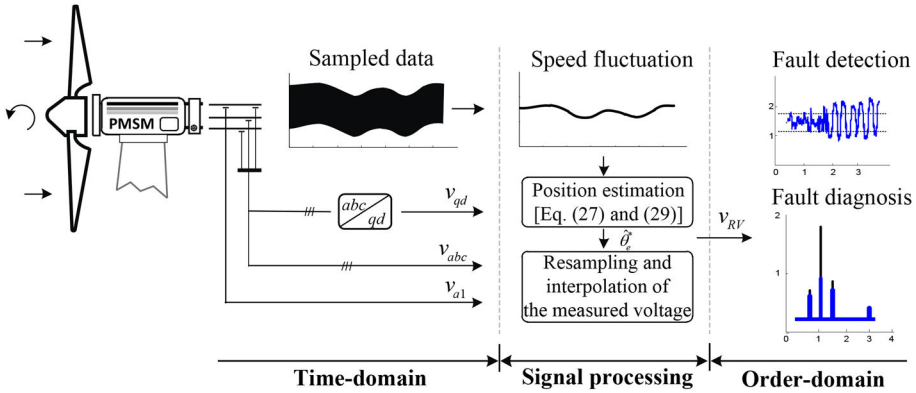

Fig. 2 *Scheme of the proposed strategy for the interturn short-circuit fault detection and isolation in PMSM*

2.3 Fault severity factor (FSF)

A reliable indicator is necessary for the right detection and quantification of the stator fault in PMSM. From (9) it can be seen that the RV is proportional to the fault severity, μ, and the fault current, i_f. Therefore, a FSF is defined for each phase winding, as follows:

$$\text{FSF} = \frac{\left|\mu\tilde{I}_f\right|}{\left|\tilde{V}_x\right|}, \tag{22}$$

with $x = a, b$, or c, where

$$\left|\mu\tilde{I}_f\right| = \frac{\left|\tilde{V}_{RVx}\right|}{\left|((r_s/2) + j\omega_e(L_s/2))\right|}.$$

To avoid false detection due to inherent asymmetries, external perturbations, and measurement errors, the FSF must be compared to a threshold limit value (J_{TH}), which is defined for the healthy PMSM condition, as follows:

$$J_{TH} = \max_{\text{nofault}} \text{FSF}. \tag{23}$$

The interturn short-circuit fault is detected when FSF > J_{TH}.

The proposed FSF requires us to know the electrical parameters of the PMSM, similar to the fault indicator proposed in the ZSVC-based method [16]. Besides, the proposed FSF allows us to detect an interturn short-circuit fault, but the fault severity will not be right if the fault occurs in one of the windings where the midpoint is not available. Therefore, the proposed strategy requires all the midpoints to be available for correct fault diagnosis.

To analyse the FSF against the variation of the fault resistance, from the seventh row of (1) the fault current for the steady-state can be expressed as follows:

$$\tilde{I}_f = \frac{\mu\tilde{V}_a}{\mu Z_f + 2r_f}, \tag{24}$$

where $Z_f = r_s + j\omega_e(L_{ls} + \mu L_M)$.

By replacing (24) into (13), the RV of the a-phase winding is given by

$$\tilde{V}_{RVa} = \mu\left(\frac{r_s}{2} + j\omega_e\frac{L_s}{2}\right)\frac{\mu\tilde{V}_a}{\mu Z_f + 2r_f}. \tag{25}$$

Next, replacing (25) into (22) with $x = a$, the FSF expressed as a function of fault resistances may now be written as

$$\text{FSF}\, r_f = \frac{1}{2}\frac{\mu}{\left|(Z_f/2) + (r_f/\mu)\right|}. \tag{26}$$

The FSF r_f obtained from the PMSM dynamic model is equivalent to the proposed FSF. Note that a large fault severity is produced by small fault resistances and a large number of shorted turns (high fault current value). On the other hand, a low fault severity is produced by high-fault resistances and a low number of shorted turns (low fault current value).

3 PMSM operating with stator fault under the non-stationary condition

To capture the maximum wind energy, the wind turbine speed is controlled by the generator-side converter [29]. The rotor speed variations produce frequency variations of electrical signals in the time-domain, which will in turn produce an error on the estimated fault severity in case that a steady-state fault diagnosis strategy is used (e.g. MCSA/MVSA). To take into account these non-stationary operating conditions, the proposed strategy is based on the OT concept. An OT method was applied in [30] for non-stationary vibration signal analysis based on a sampling of vibration signals synchronised with the rotor shaft speed. Based on this approach, some strategies were developed to detect defects on moving parts of the machine such as rotor imbalance [31] and bearing faults [32]. In this work, the OT concept is applied to detect and isolate an interturn short-circuit fault in the direct-drive PMSM-based WECS. A general scheme is shown in Fig. 2.

Basically, the proposed strategy is divided into the following three stages:

(i) *Time-domain*: the stator phase voltages, $\boldsymbol{v}_{abcs}$, and one midpoint voltage of any phase windings are measured (in this case the semi-windings voltage measurement, v_{a1}, see Fig. 2). These voltages in time-domain are acquired at the fixed sampling frequency.
(ii) *Signal processing*: signal processing is applied for measured voltages to reject the effects of the non-stationary speed operating conditions.
(iii) *Order-domain*: the analysis of voltage frequency spectra is performed in the order domain for the interturn short-circuit fault detection and isolation.

The OT signal processing is applied to reject the detrimental effects of the non-stationary operating conditions. For this, the instantaneous rotor position is required, which is commonly obtained by using different sensors such as piezoelectric sensors or accelerometers. In this work, the rotor position, θ_r, is estimated through the phase voltages, $\boldsymbol{v}_{abcs}$, that are transformed into the dq stationary reference frame. Note that, from (1), the output voltage for the no-loaded condition ($\boldsymbol{i}_{abc} = 0$) is directly the induced back-EMF. Therefore, to avoid the use of an external sensor, the angular rotor position relative to the stator axis, θ_e, can be estimated from the measured voltages as follows [33]:

$$\hat{\theta}_e \simeq \text{atan2}(v_d, v_q). \tag{27}$$

where $\theta_e = P\theta_r$ with P the number of pole pairs.

In case that the PMSM is loaded ($\boldsymbol{i}_{abc} \neq 0$), the output voltage will be different from the back-EMF due to the voltage drop in the

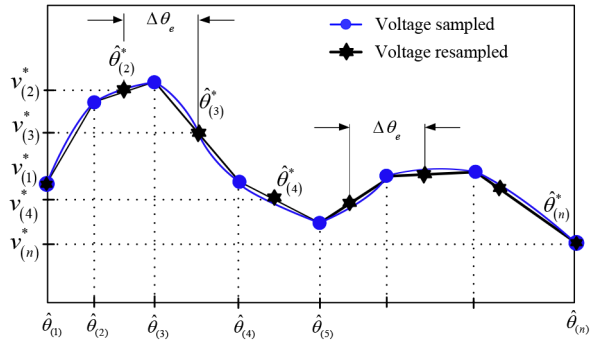

Fig. 3 *Data resampling scheme*

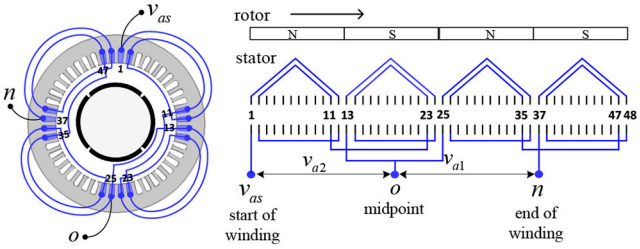

Fig. 4 *Distributed winding of the PMSM prototype*

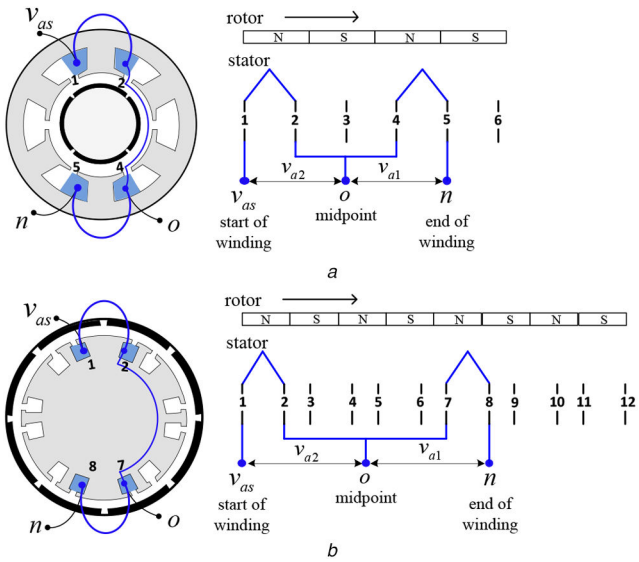

Fig. 5 *PMSM with concentrated windings*
(a) Double-layer, ***(b)*** Single-layer fractional pitch windings

stator resistance and inductances. However, the difference between the relative position of the back-EMF and the output voltage will be constant and small magnitude [32]. Thus, the rotor speed may be estimated from (27) as

$$\hat{\omega}_{\mathrm{e}}(k) = \frac{\hat{\theta}_{\mathrm{e}}(k) - \hat{\theta}_{\mathrm{e}}(k-1)}{\Delta_T}, \tag{28}$$

where Δ_T is the sample/hold interval.

From (27), the angular rotor position relative to the stator axis, $\hat{\theta}_{\mathrm{e}}$, is sampled with a fixed sampling frequency, $t = t_0, t_1, \ldots, t_n$, as follows:

$$\hat{\boldsymbol{\theta}}_{\mathrm{e}} = \left[\hat{\theta}_{(1)} \quad \hat{\theta}_{(2)} \quad \hat{\theta}_{(3)} \quad \cdots \quad \hat{\theta}_{(n)}\right]. \tag{29}$$

From (29), the rotor shaft position but at fixed increments $\left(\Delta\hat{\theta}_{\mathrm{e}}\right)$, are obtained as follows:

$$\begin{aligned}\hat{\boldsymbol{\theta}}^{*}_{\mathrm{e}} &= \left[\hat{\theta}^{*}_{(1)} \quad \hat{\theta}^{*}_{(2)} \quad \hat{\theta}^{*}_{(3)} \quad \cdots \quad \hat{\theta}^{*}_{(n)}\right] \\ &= \left[\hat{\theta}_{(1)} \quad \hat{\theta}_{(1)} + \Delta\hat{\theta}_{e} \quad \hat{\theta}_{(1)} + 2\Delta\hat{\theta}_{\mathrm{e}} \quad \cdots \quad \hat{\theta}_{(n)}\right],\end{aligned} \tag{30}$$

where $\hat{\theta}^{*}_{(e)}$ is the estimated angular position with equally-spaced angular position increments at $\Delta\hat{\theta}_{\mathrm{e}} = \left(\hat{\theta}_{(n)} - \hat{\theta}_{(1)}\right)/(n-1)$.

Therefore, from (29) and (30), the resampled voltage signal is obtained through a linear interpolation method, as follows:

$$\boldsymbol{v}^{*} = \mathrm{interp}\left(\hat{\theta}_{\mathrm{e}}, v, \hat{\theta}^{*}_{\mathrm{e}}\right), \tag{31}$$

where

$$\boldsymbol{v}^{*} = \left[v^{*}_{(1)} \quad v^{*}_{(2)} \quad v^{*}_{(3)} \quad \cdots \quad v^{*}_{(n)}\right].$$

A data resampling scheme is shown in Fig. 3. The components of vector, $\boldsymbol{v}^{*}$, corresponding to the components of $\hat{\theta}^{*}_{\mathrm{e}}$, are determined by interpolation within vectors $\hat{\boldsymbol{\theta}}_{\mathrm{e}}$ and $\boldsymbol{v}$. Once applied the signal processing operation, the resampled voltage, $\boldsymbol{v}^{*}$, is normalised as a function of the estimated rotor speed, $\hat{\omega}_{\mathrm{e}}$. Since (31) is a periodic signal at, $\hat{\theta}^{*}_{\mathrm{e}}$, angular rotor positions, this resampled voltage can be analysed through the fault diagnosis techniques for the steady-state condition. Furthermore, the estimated rotor speed is used for the normalisation of the instantaneous voltages to reduce the effects of speed variations produced in wind turbines. In this way, variations in induced back-EMF produced by changes in rotor speed are cancelled and the resulting signals have practically constant amplitude.

4 Experimental test and results

To validate the proposed signal-based method, several experimental tests were performed using a three-phase PMSM prototype with modified stator windings. This winding modification allows adjusting the fault severity from the first, second, third, fourth, fifth, and tenth turns of one coil of the phase winding (0.7–7% turns with respect to the total turns of the complete phase winding).

The midpoint connection can be made in PMSMs with both, distributed or concentrated windings if there is a geometric symmetry between the two halves of the winding (semi-windings). The midpoint connections for different winding configurations are shown in Figs. 4 and 5. The spatial distribution of the *a*-phase coils in the stator slots of the PMSM used for the experimental results is shown in Fig. 4. This PMSM has distributed windings with two coils per pole. Each 'start' and 'end' of the coils can be accessible from a terminal box. In particular, the terminals 1, 11, 13, 23, 25, 35, 37, and 47 correspond to the poles of *a*-phase and can be handled for the winding configurations. Therefore, the midpoint '*o*' can be accessible in the connection of two poles, as can be seen in Fig. 4. On the other hand, the winding distribution and midpoint connections for two PMSMs with concentrated windings are shown in Fig. 5. Fig. 5*a* corresponds to a PMSM with four poles and double-layer fractional pitch windings and Fig. 5*b* corresponds to an outer-rotor PMSM with eight poles and single-layer fractional pitch windings and unequal teeth structure.

The test bench developed and built for experimental validation is composed of a voltage-source power electronic converter to continuously control the speed of a three-phase induction machine directly coupled to the PMSM. The PMSM prototype parameters are shown in Table 1.

Fig. 6 shows an image of the experimental platform that has been assembled. A Yokogawa OR300 oscillographic recorder at a sampling frequency of $f_{\mathrm{S}} = 8\,\mathrm{kS/s}$ was used for measuring phase voltages, v_{as}, and the semi-winding voltage, v_{a1}. In the same figure, it is shown a connection scheme that indicates the semi-winding voltage, v_{a1}, measured between the 'midpoint terminal' and the 'end' of the winding. To safeguard the stator winding against high fault-currents, the experimental tests were performed for a short

Table 1 PMSM parameters

Characteristic	Symbol	Value	Units
rated power	P_N	7.5	HP
rated voltage	V_N	380	V
rated current	I_N	11.8	A
rated speed	ω_r	1500	RPM
permanent magnet flux	ψ_{pm}	0.78	Wb
stator resistance	r_s	0.8	Ω
stator inductance	L	2.5×10^{-3}	H
number of pole pairs	P	2	—
connection windings	—	—	series
turns/coil	—	—	18
turns/phase	—	—	144

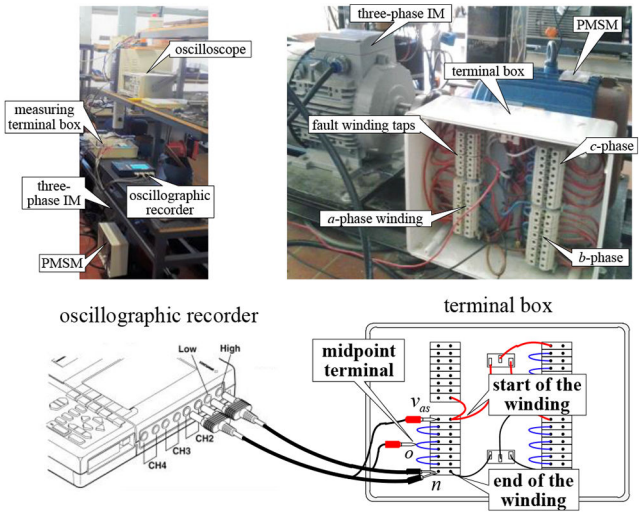

Fig. 6 *Image of the experimental setup and PMSM prototype*

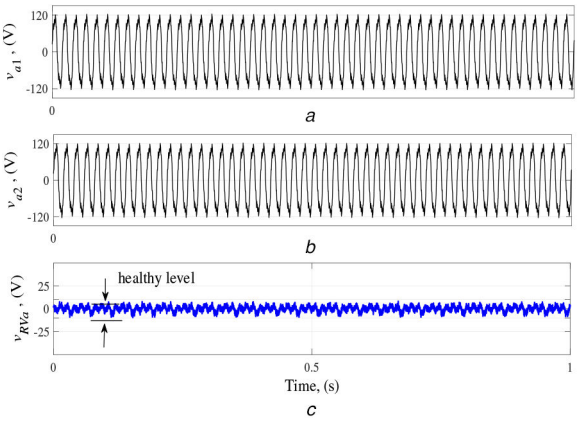

Fig. 7 *Healthy PMSM at fixed-speed operation under symmetric load condition*
(a) v_{a1}, ***(b)*** v_{a2}, ***(c)*** v_{RVa}

time (~4–8 s), and also an external resistor, $r_f = 149\,m\Omega$, was connected between the terminals of the shorted turns. The current fault was measured by using Current Clamp Probes Fluke i200 on the 'measuring terminal box'. Finally, the acquired data were analysed on a personal computer.

The experimental test that was carried out is mentioned below

(i) *Steady-state and symmetrical load condition*: a three-phase resistance load, $r_{abc} = 23.6\,\Omega$, was connected to the PMSM terminals to obtain the rated current. In addition, different rotor speeds conditions were evaluated, 600, 900, 1200, and 1500 RPM.
(ii) *Transient and asymmetrical load condition*: to evaluate the robustness of the proposed strategy, the load imbalance was produce by connecting on the terminals of the three-phase PMSM prototype, $r_a = 23.6\Omega$, $r_b = 20\Omega$, and $r_c = 23.5\Omega$. Asymmetric load condition causes an unbalance of stator currents of $7\%\tilde{I}_{sn}/\tilde{I}_{sp}$; such a case could occur for a power electronics fault in the generator-side inverter in WECS or due to supply voltage unbalance for a PMSM working as a motor.

Fig. 7 shows experimental results for a healthy PMSM operating at fixed-speed under symmetric load conditions. Fig. 7*a* shows the voltage measurement of v_{a1}. In this application, v_{as} and v_{a1} were measured and, the semi-winding voltage, v_{a2}, is calculated by: $v_{a2} = v_{as} - v_{a1}$, as it is shown in Fig. 7*b*. Since the partial voltage drop on both semi-windings of the *a*-phase is caused by the current, i_a, through the stator resistance and the magnetising inductance [see in (8)], the voltage v_{RV_a} will be zero or close to zero, even for healthy PMSM with asymmetric load condition. This resulting signal is shown in Fig. 7*c*. Note that the healthy level for PMSM without stator fault is a non-zero signal due to inherent asymmetries and measurement errors.

Fig. 8 shows the voltage frequency spectra at 1500 RPM for healthy PMSM. It is possible to see that the magnitudes of the frequency components of v_{a1} are equal to half of the magnitudes components of v_a shown in Figs. 8*b* and *a*, respectively. Fig. 8*c* shows the frequency spectrum of v_{RV_a}. As can be appreciated, frequency components as sidebands around the fundamental component appear according to: $f_f = f_s(1 \pm k/P)$, where k is any integer number. The pattern of f_f can be used to monitor other fault types such as eccentricity, asymmetric damage, or demagnetisation in the permanent magnets [12, 34].

The stator voltages for PMSM with ten short circuited turns at $t = 1.2\,s$ is presented in Fig. 9. The voltage, v_{a1}, of the healthy semi-winding is shown in Fig. 9*a*. It can be seen that the voltage amplitude remained invariant during all the experimental tests. The voltage, v_{a2}, on the faulty semi-winding is shown in Fig. 9*b*. Unlike the healthy semi-winding, the voltage amplitude of v_{a2} is reduced at the moment the fault is triggered. Fig. 9*c* shows the v_{RV_a} resulting signal. It is clear that amplitude increases when a stator fault is triggered. Therefore, a threshold limit is required to indicate the faulty PMSM condition. Additionally, a note about the details of voltages that the angular phase of v_{RV_a} holds on the same angular phase of the faulty semi-winding. Since the amplitude of v_{RV_a} is proportional to μi_f [see in (9)], this signal is used to estimate the stator fault severity in Section 2.3.

To evaluate the robustness of the proposed strategy several experimental tests under asymmetrical load and transient conditions were performed. Fig. 10 shows the spectra amplitudes for the PMSM operating with ten short-circuited turns under different rotor speed and asymmetrical load conditions. As can be seen the amplitudes of both, v_{RV_a} and fault current i_f, increase as the rotor speed increases. Note that the pattern of frequencies of the fault current is similar to the frequencies of the phase voltage spectrum, as discussed in [19].

The voltages v_{a1}, v_{a2}, and v_{RVa} for PMSM with speed fluctuation are shown in Figs. 11*a–c*, respectively. Fig. 11*d* shows the amplitude spectrum of v_{RVa}. The non-stationary conditions produce frequencies fluctuations, which then cause smearing of RPM-dependent spectral components. This speed fluctuations produce an error in the peak value of the measurement of the voltage. Therefore, the fault detection strategies based on steady-state operation are not suitable [spectrum details are exposed in the box in Fig. 11*d*].

Fig. 12 shows the estimated rotor speed from the measured voltages [see in (28)]. Three experimental tests are presented for rotor speed with low and middle fluctuations and a speed ramp.

The estimated and resampled angular rotor position [see in (29) and (30), respectively] are superimposed to make evident the rotor-angular increase differences under non-stationary conditions, as shown in Fig. 13. It is clear that variations in rotor speed cause non-linear increments in the rotor position. To reject the detrimental effects of the non-stationary speed conditions, a signal

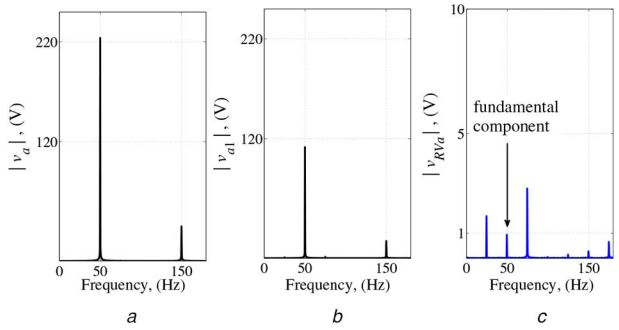

Fig. 8 *Voltage spectra for healthy PMSM at 1500 rpm*
(a) Spectrum of v_{as}, ***(b)*** Spectrum of v_{a1}, ***(c)*** Spectrum of $v_{\mathrm{RV}a}$

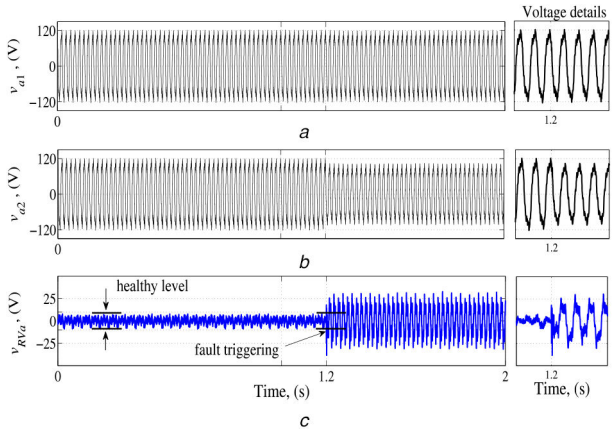

Fig. 9 *Faulty PMSM under symmetric load condition at 1500 rpm*
(a) v_{a1}, ***(b)*** v_{a2}, ***(c)*** $v_{\mathrm{RV}a}$

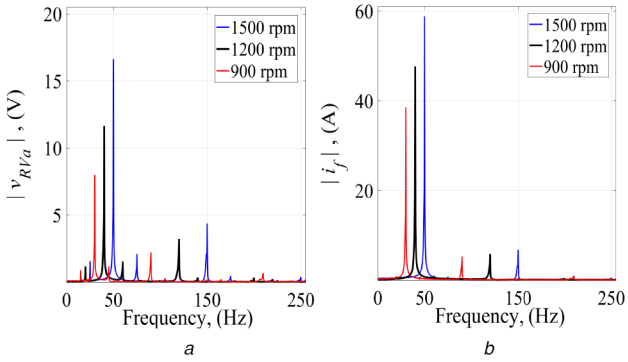

Fig. 10 *Frequency spectra of the RV and fault current, i_f, for different rotor speeds*

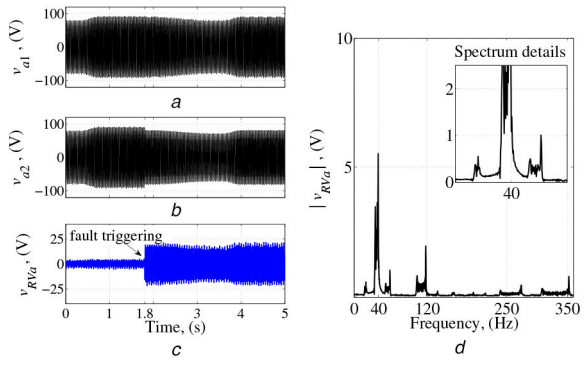

Fig. 11 *Faulty PMSM under asymmetric load and non-stationary speed conditions*
(a) v_{a1}, ***(b)*** v_{a2}, ***(c)*** $v_{\mathrm{RV}a}$, ***(d)*** Spectrum of $v_{\mathrm{RV}a}$

processing of the measured voltages was performed, such as explained in detail in Section 3. In this proposed strategy, the

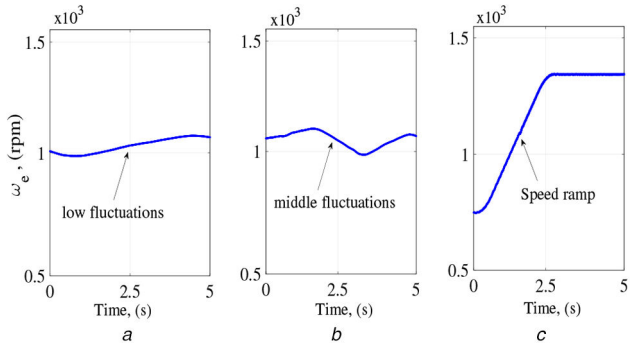

Fig. 12 *Variable speed*
(a) Case 1, ***(b)*** Case 2, ***(c)*** Case 3: speed ramp

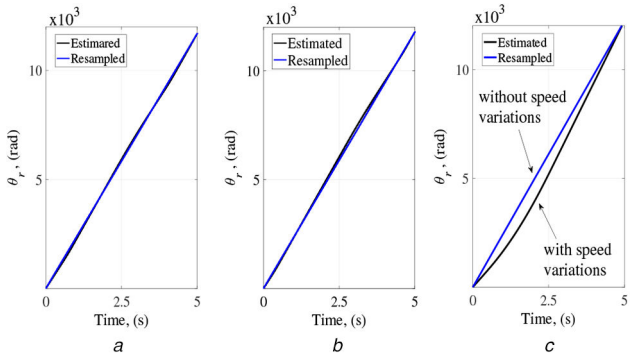

Fig. 13 *Estimated and resampled rotor position from*
(a) Case 1, ***(b)*** Case 2, ***(c)*** Case 3: speed ramp

voltages sampling at fixed frequency is resampled by a synchronous sampling frequency at fixed increments of the rotor angular position, and then they are normalised as a function of the rotor speed. The time axis is replaced by a number of periods, and the voltage spectrum result has a frequency axis that is physically scaled in orders.

Once the voltages are resampled and normalised with the rotor speed, the resulting signals are shown in Figs. 14*a–c*. The spectrum of $v_{\mathrm{RV}a}$ is shown in Fig. 14*d*. As can be seen, the voltage signals variation from non-stationary conditions is identical to those obtained in steady-state conditions, as shown in Figs. 8 and 10.

Figs. 15*a–c* show the spectra of $v_{\mathrm{RV}a}$ for healthy PMSM, one and two short-circuited turns, respectively.

Also, Figs. 16*a–c* show the spectra for three, five, and ten short-circuited turns. The voltage spectra for the healthy and faulty PMSM are superimposed for amplitude comparison. It should be noted that the sidebands around the fundamental component practically remained invariant for all case tests. However, only the fundamental component increases when the stator fault severities also increase. Based on the exposed results, the proposed strategy is sensitive for detecting stator faults from at least one short-circuited turn.

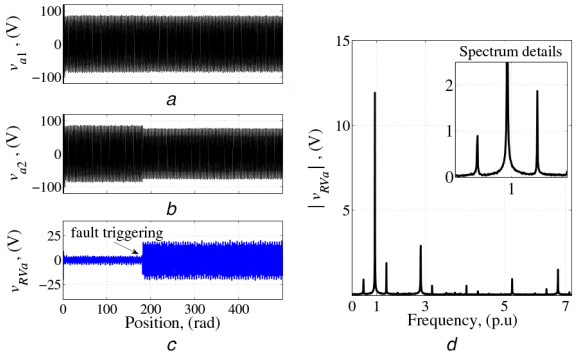

Fig. 14 *Resampled and normalised voltages with the rotor speed*
(a) v_{a1}, ***(b)*** v_{a2}, ***(c)*** v_{RVa}, ***(d)*** Spectrum of v_{RVa}

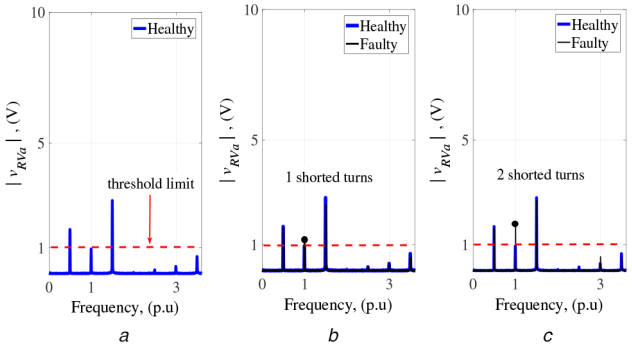

Fig. 15 *Spectra of* v_{RVa}
(a) Healthy winding, ***(b)*** 0.69% short-circuited winding, ***(c)*** 1.39% short-circuited winding

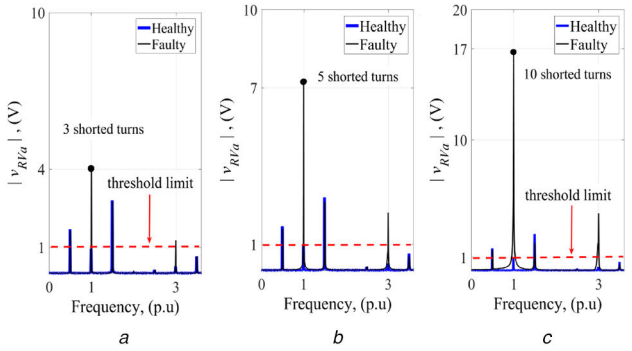

Fig. 16 *Spectra of* v_{RVa} *for different short-circuited winding severities*
(a) 2.08%, ***(b)*** 3.47%, ***(c)*** 6.94%

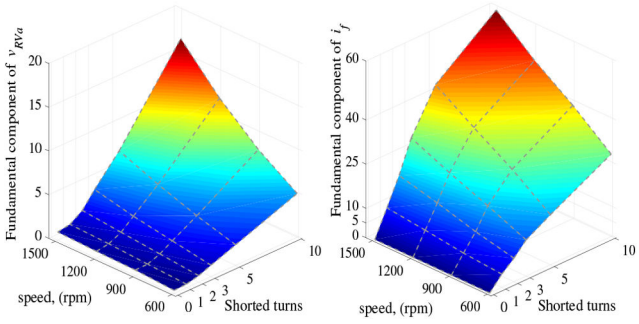

Fig. 17 v_{RVa} *and* i_f *for different rotor speeds and fault severities*

Fig. 17 shows the surface plots for several angular speeds and fault severities of the fundamentals component of v_{RV_a} (left picture) and fault current, i_f (right picture).

On the other hand, Figs. 18*a–c* show the measured voltages on semi-windings of the three phases and the v_{RV} resulting signals. As can be seen, the RV obtained from any stator phase can be used as an alarm to indicate stator faults. However, the voltages resulting

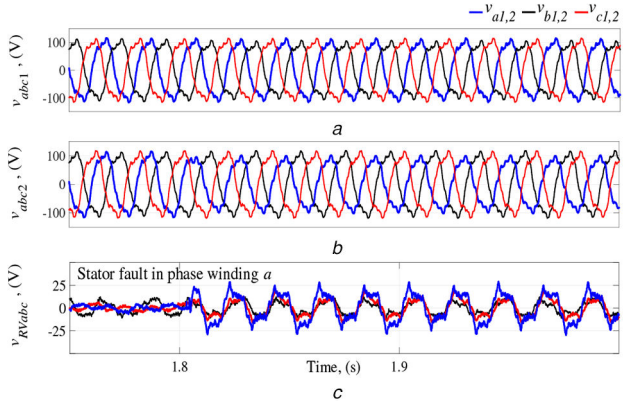

Fig. 18 *Semi-winding voltages and RVs from the a-, b- and c-phase winding*
(a) v_{abc1}, ***(b)*** v_{abc2}, ***(c)*** v_{RVabc}

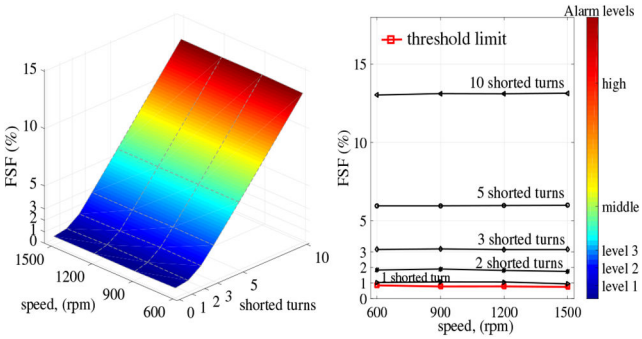

Fig. 19 *FSF for different rotor speeds and fault severities*

from the healthy phases, v_{RV_b} and v_{RV_c}, have lower amplitudes than the voltage resulting from the damaged phase, v_{RV_a} [see in (11) and (12)]. In addition, the RV obtained from any winding phase hold the same angular phase as the faulty winding phase voltage. This is one of the highlights of the proposed signal-based strategy since an interturn short-circuit faults can be detected and located from the voltage measured on phase winding *a*, *b*, or *c*.

To analyse the performance of the FSF, Fig. 19 shows the surface plot for several angular speeds and fault severities (left picture). The contour lines of the surface plot (right picture) show the threshold limit for healthy PMSM and the alarm levels set. As can be seen, the magnitude of the threshold limit holds on the same value without taking into account the angular speed. The FSF increases as the fault severity increases. Thus, this indicator can be compared to the threshold limit value to trigger an early alarm.

5 Conclusion

In this paper, a new signal-based method for interturn short-circuit fault detection and isolation in PMSM using the midpoint voltage of the stator winding was proposed. A three-phase PMSM dynamic model with partitioned stator windings was developed to demonstrate analytically the effects produced by stator faults. From this extended PMSM model, a RV is obtained by subtracting the voltages of the two semi-windings connected in series of the same phase, allowed to decouple the effects of asymmetric load condition. To decouple the effects of the non-stationary speed, the voltages sampled at fixed frequency are resampled but at fixed increments of the rotor shaft angular position. In this work, the angular rotor position is estimated from the measured voltages at terminals of the PMSM, without the need for an additional external speed sensor. Therefore, the performance of the proposed strategy is not affected by asymmetric load or non-stationary speed conditions.

Several experimental tests have demonstrated that the RV allows detecting an incipient interturn short-circuit fault. Since the fault severities increase only the fundamental component of RV, fault diagnosis can be carried out by monitoring the changes of RV

spectrum components. The stator fault is detected once the FSF exceeds the threshold limit pre-set for healthy PMSM, even if the RV of the faulty winding is not available. However, since the FSF is defined for each phase winding, the strategy requires all the phase midpoints to be available for correct quantification of the fault severity.

Based on the exposed experimental results, the high sensitivity of the proposed strategy for detecting an incipient interturn short-circuit fault in PMSM has been demonstrated (from at least one-turn fault). Similar to ZSCV-based methods, the neutral point of the stator windings is required and also the midpoint of all phase windings. Although the midpoint of the windings is not available in many cases in practice, it is easy to make the midpoint accessible within a phase by connecting an additional terminal during the winding or rewinding the manufacturing process. Despite the modification of the stator windings, the addition of the midpoint in each phase is less invasive than other techniques proposed for fault diagnosis such as the insertion of search coils around each tooth to measure air-gap flux density. As further works, we will investigate the effects of the static eccentricity on midpoint voltage to quantify stator faults and rotor eccentricities.

6 Acknowledgments

This work was financial support by Consejo Nacional de Investigaciones Científicas y Técnicas (CONICET), Argentina, and was partially supported by the Universidad Nacional de Misiones (UNaM) and Universidad Nacional de Río Cuarto (UNRC).

7 References

[1] Alexandrova, Y., Semken, R. S., Pyrhonen, J.: 'Permanent magnet synchronous generator design solution for large direct-drive wind turbines: thermal behavior of the LC DD-PMSG', *Appl. Therm. Eng.*, 2014, **65**, (1–2), pp. 554–563

[2] Sekerak, P., Hrabovcova, V., Pyrhonen, J., *et al.*: 'Comparison of synchronous motors with different permanent magnet and winding types', *IEEE Trans. Magn.*, 2013, **49**, (3), pp. 1256–1263

[3] Cheng, M., Zhu, Y.: 'The state of the art of wind energy conversion systems and technologies: a review', *Energy Convers. Manage.*, 2014, **88**, pp. 332–347

[4] Yaramasu, V., Dekka, A., Durán, M.J., *et al.*: 'PMSG-based wind energy conversion systems: survey on power converters and controls', *IET Electr. Power Appl.*, 2017, **11**, (6), pp. 956–968

[5] Hashemian, H.: 'State-of-the-art predictive maintenance techniques', *IEEE Trans. Instrum. Meas.*, 2011, **60**, (1), pp. 226–236

[6] Grubic, S., Aller, J.M., Bin, L., *et al.*: 'A survey on testing and monitoring methods for stator insulation systems of low-voltage induction machines focusing on turn insulation problems', *IEEE Trans. Ind. Electron.*, 2008, **55**, (12), pp. 4127–4136

[7] Bellini, A., Filippetti, F., Tassoni, C., *et al.*: 'Advances in diagnostic techniques for induction machines', *IEEE Trans. Ind. Electron.*, 2008, **55**, (12), pp. 4109–4126

[8] Riba Ruiz, J.R., Rosero, J.A., Espinosa, A.G., *et al.*: 'Detection of demagnetization faults in permanent-magnet synchronous motors under nonstationary conditions', *IEEE Trans. Magn.*, 2009, **45**, (7), pp. 2961–2969

[9] Lee, S.B., Hong, J.M.: 'Apparatus and method for diagnosing permanent magnet demagnetization of permanent magnet synchronous motor, and apparatus for driving permanent magnet synchronous motor', Patent, vol. 20110260748, 2011. Available at http://www.faqs.org/patents/app/20110260748

[10] Haddad, R.Z., Strangas, E.G.: 'On the accuracy of fault detection and separation in permanent magnet synchronous machines using MCSA/MVSA and LDA', *IEEE Trans. Energy Convers.*, 2016, **31**, (3), pp. 924–934

[11] Zafarani, M., Bostanci, E., Qi, Y., *et al.*: 'Inter-turn short circuit faults in permanent magnet synchronous machines: an extended review and comprehensive analysis', *IEEE J. Emerging Sel. Top. Power Electron.*, 2018, **6**, pp. 2173–2191

[12] Duan, Y., Toliyat, H.: 'A review of condition monitoring and fault diagnosis for permanent magnet machines'. Power and Energy Society General Meeting, 2012 IEEE, San Diego, CA, 2012, pp. 1–4

[13] Liu, W., Liu, L., Chung, I.-Y., *et al.*: 'Modeling and detecting the stator winding fault of permanent magnet synchronous motors', *Simul. Modelling Pract. Theory*, 2012, **27**, pp. 1–16

[14] Gandhi, A., Corrigan, T., Parsa, L.: 'Recent advances in modeling and online detection of stator interturn faults in electrical motors', *IEEE Trans. Ind. Electron.*, 2011, **58**, (5), pp. 1564–1575

[15] Urresty, J., Riba Ruiz, J.R., Delgado, M., *et al.*: 'Detection of demagnetization faults in surface-mounted permanent magnet synchronous motors by means of the zero-sequence voltage component', *IEEE Trans. Energy Convers.*, 2012, **27**, (1), pp. 42–51

[16] Hang, J., Zhang, J., Cheng, M., *et al.*: 'Online interturn fault diagnosis of permanent magnet synchronous machine using zero sequence components', *IEEE Trans. Power Electron.*, 2015, **30**, (12), pp. 6731–6741

[17] Moosavi, S., Djerdir, A., Amirat, Y., *et al.*: 'Demagnetization fault diagnosis in permanent magnet synchronous motors: a review of the state-of-the-art', *J. Magn. Magn. Mater.*, 2015, **391**, pp. 203–212

[18] Jeong, H., Moon, S., Kim, S.W.: 'An early stage interturn fault diagnosis of PMSMs by using negative-sequence components', *IEEE Trans. Ind. Electron.*, 2017, **64**, (7), pp. 5701–5708

[19] Saavedra, H., Urresty, J.-C., Riba, J.-R., *et al.*: 'Detection of interturn faults in PMSMs with different winding configurations', *Energy Convers. Manage.*, 2014, **79**, pp. 534–542

[20] Mazzoletti, M.A., Bossio, G.R., Angelo, C.D., *et al.*: 'Efectos del cortocircuito entre espiras en máquinas síncronas de imanes permanentes'. Biennial Congress of Argentina (ARGENCON), 2014 IEEE, Bariloche, Argentina, June 2014, pp. 531–536

[21] Obeid, N.H., Battiston, A., Boileau, T., *et al.*: 'Early intermittent interturn fault detection and localization for a permanent magnet synchronous motor of electrical vehicles using wavelet transform', *IEEE Trans. Transp. Electrification*, 2017, **3**, (3), pp. 694–702

[22] Fang, J., Sun, Y., Wang, Y., *et al.*: 'Improved ZSVC-based fault detection technique for incipient stage inter-turn fault in PMSM', *IET Electr. Power Appl.*, 2019, **13**, (12), pp. 2015–2026

[23] Rosero, J., Romeral, L., Ortega, J., *et al.*: 'Short-circuit detection by means of empirical mode decomposition and Wigner-Ville distribution for PMSM running under dynamic condition', *IEEE Trans. Ind. Electron.*, 2009, **56**, (11), pp. 4534–4547

[24] Aubert, B., Régnier, J., Caux, S., *et al.*: 'Kalman-filter-based indicator for online interturn short circuits detection in permanent-magnet synchronous generators', *IEEE Trans. Ind. Electron.*, 2015, **62**, (3), pp. 1921–1930

[25] Da, Y., Shi, X., Krishnamurthy, M.: 'A new approach to fault diagnostics for permanent magnet synchronous machines using electromagnetic signature analysis', *IEEE Trans. Power Electron.*, 2013, **28**, (8), pp. 4104–4112

[26] Zeng, C., Huang, S., Yang, Y., *et al.*: 'Inter-turn fault diagnosis of permanent magnet synchronous machine based on tooth magnetic flux analysis', *IET Electr. Power Appl.*, 2018, **12**, (6), pp. 837–844

[27] Mazzoletti, M.A., Bossio, G.R., De Angelo, C.H.: 'A strategy for interturn short-circuit fault detection in PMSM with partitioned stator windings'. 2017 XVII Workshop on Information Processing and Control (RPIC), Mar del Plata, Argentina, September. 2017, pp. 1–7

[28] Krause, P., Wasynczuk, O., Sudhoff, S., *et al.*: '*Analysis of electric machinery and drive systems*' (IEEE Press, New Jersey, USA, 2013, 3rd edn.)

[29] Hong, C.-M., Chen, C.-H., Tu, C.-S.: 'Maximum power point tracking-based control algorithm for PMSG wind generation system without mechanical sensors', *Energy Convers. Manage.*, 2013, **69**, pp. 58–67

[30] Fyfe, K.R., Munck, E.D.S.: 'Analysis of computed order tracking', *Mech. Syst. Signal Process.*, 1997, **11**, (2), pp. 187–205

[31] Abouhnik, A., Albarbar, A.: 'Wind turbine blades condition assessment based on vibration measurements and the level of an empirically decomposed feature', *Energy Convers. Manage.*, 2012, **64**, pp. 606–613

[32] Pezzani, C.M., Bossio, J.M., Castellino, A.M., *et al.*: 'A PLL-based resampling technique for vibration, analysis in variable-speed wind turbines with PMSG: A bearing fault case', *Mech. Syst. Signal Process.*, 2017, **85**, pp. 354–366

[33] Zhao, Y., Wei, C., Zhang, Z., *et al.*: 'A review on position/speed sensorless control for permanent-magnet synchronous machine-based wind energy conversion systems', *IEEE J. Emerging Sel. Top. Power Electron.*, 2013, **1**, (4), pp. 203–216

[34] Bossio, J.M., Ruschetti, C.R., Bossio, G.R., *et al.*: 'Rotor fault diagnosis in PMSM using the midpoint voltage of windings', *IET Electr. Power Appl.*, 2019, **14**, (2), pp. 256–261

8 Appendix

The self and mutual inductance of PMSM model may be defined as the winding function of semi-winding x of the a-phase

$$w_{x_{|a}} = \begin{cases} N_x \cos(2\phi_m), & 0 < \phi_m \leq \pi \\ 0 & \text{other} \end{cases}$$

The winding function of semi-winding y of the a-phase

$$w_{y_{|a}} = \begin{cases} N_y \cos(2\phi_m) & \pi < \phi_m \leq 2\pi \\ 0 & \text{other} \end{cases}$$

By using (6), $x = y$ to calculate the self-inductance. Substitution of w_x and w_y into (6), the self-inductance of the a-phase semi-windings may be expressed as $L_{xx} = L_{yy} = 1/2L_s$. Considering the winding functions of the defined semi-windings, the mutual-inductances are a function of the rotor position relative to the stator and, thus, the contribution of the flux linkages of the semi-winding x at a position of the semi-winding y is null, $L_{xy} = 0$.

To calculate the mutual-inductance relationships between semi-windings of the b-phase, the winding function is defined by the winding function of semi-winding x of the b-phase

$$w_{x_{|_b}} = \begin{cases} N_x \cos[2(\phi_m - (\pi/3))], & \pi/3 < \phi_m \le 4\pi/3 \\ 0 & \text{other}. \end{cases}$$

The winding function of semi-winding y of the b-phase

$$w_{y_{|_b}} = \begin{cases} N_y \cos[2(\phi_m - (4\pi/3))], & 4\pi/3 < \phi_m \le 2\pi \cup \\ & 0 < \phi_m \le \pi/3 \\ 0 & \text{other}. \end{cases}$$

By using (6), the mutual inductance between $w_{x_{|_a}}$ and $w_{x_{|_b}}$ is $L_{xy} = aL_{\mathrm{M}}$. Also, the mutual inductance between $w_{x_{|_a}}$ and $w_{y_{|_b}}$ is $L_{yx} = bL_{\mathrm{M}}$.

The windings coupling factors are defined as $a = -(\sqrt{3}/4) - (\pi/3)$, and $b = (\sqrt{3}/4) - (\pi/6)$, [see in (4)].

To calculate the mutual inductance relationships between semi-windings of the c-phase, the winding function is defined by the following:

The winding function of semi-winding x of the c-phase

$$w_{x_{|_c}} = \begin{cases} N_x \cos[2(\phi_m - (2\pi/3))], & 2\pi/3 < \phi_m \le 5\pi/3 \\ 0 & \text{other}. \end{cases}$$

The winding function of semi-winding y of the c-phase

$$w_{y_{|_c}} = \begin{cases} N_y \cos[2(\phi_m - (5\pi/3))], & 5\pi/3 < \phi_m \le 2\pi \cup \\ & 0 < \phi_m \le 2\pi/3 \\ 0 & \text{other}. \end{cases}$$

Thus, the mutual inductance between $w_{x_{|_a}}$ and $w_{x_{|_c}}$ can be written as $L_{xy} = bL_{\mathrm{M}}$. Also, the mutual inductance between $w_{x_{|_a}}$ and $w_{y_{|_c}}$ as $L_{yx} = aL_{\mathrm{M}}$.